HHS Public Access

Author manuscript

J Control Release. Author manuscript; available in PMC 2019 June 10.

Published in final edited form as:

J Control Release. 2018 June 10; 279: 292–305. doi:10.1016/j.jconrel.2018.04.026.

Multi-modal characterization of vasculature and nanoparticle accumulation in five tumor xenograft models

Einar Sulheim[1,2], **Jana Kim**[3,4], **Annemieke van Wamel**[1], **Eugene Kim**[3], **Sofie Snipstad**[1], **Igor Vidic**[1], **Ingeborg Hovde Grimstad**[1], **Marius Widerøe**[3], **Sverre H Torp**[5,6], **Steinar Lundgren**[7,8], **David J Waxman**[9], and **Catharina de Lange Davies**[1]

[1]Department of Physics, Faculty of Natural Sciences, The Norwegian University of Science and Technology (NTNU), Trondheim, Norway

[2]Department of Biotechnology and Nanomedicine, SINTEF AS, Trondheim, Norway

[3]Department of Circulation and Medical Imaging, Faculty of Medicine and Health Sciences, NTNU, Trondheim, Norway

[4]Department of Radiology and Nuclear Medicine, St. Olav's University Hospital, Trondheim, Norway

[5]Department of Laboratory Medicine, Children's and Women's Health, NTNU, Trondheim, Norway

[6]Department of Pathology, St. Olav's University Hospital, Trondheim, Norway

[7]Department of Oncology, St. Olav's University Hospital, Trondheim, Norway

[8]Department of Cancer Research and Molecular Medicine, Faculty of Medicine, NTNU, Trondheim, Norway

[9]Department of Biology, Boston University, Boston, MA, 02215USA

Abstract

Preclinical research has demonstrated that nanoparticles and macromolecules can accumulate in solid tumors due to the enhanced permeability and retention effect. However, drug loaded nanoparticles often fail to show increased efficacy in clinical trials. A better understanding of how tumor heterogeneity affects nanoparticle accumulation could help elucidate this discrepancy and help in patient selection for nanomedicine therapy. Here we studied five human tumor models with varying morphology and evaluated the accumulation of 100 nm polystyrene nanoparticles. Each tumor model was characterized *in vivo* using micro-computed tomography, contrast-enhanced ultrasound and diffusion-weighted and dynamic contrast-enhanced magnetic resonance imaging. *Ex vivo*, the tumors were sectioned for both fluorescence microscopy and histology. Nanoparticle uptake and distribution in the tumors were generally heterogeneous. Density of functional blood vessels measured by fluorescence microscopy correlated significantly ($p = 0.0056$) with

Corresponding author: einar.sulheim@ntnu.no.

nanoparticle accumulation and interestingly, inflow of microbubbles measured with ultrasound also showed a moderate but significant ($p = 0.041$) correlation with nanoparticle accumulation indicating that both amount of vessels and vessel morphology and perfusion predict nanoparticle accumulation. This indicates that blood vessel characterization using CEUS or other methods could be valuable for patient stratification for treatment with nanomedicines.

Graphical Abstract

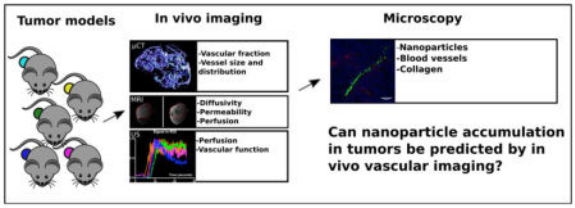

Keywords

Tumor vasculature; nanoparticles; MRI; ultrasound; microCT; microscopy; tumor characterization

Introduction

Nanoparticles (NPs) can accumulate in solid tumors due to a combined effect of leaky blood vessels and non-functional lymphatic drainage termed the enhanced permeability and retention (EPR) effect[1]. For the last three decades, NPs have been developed with the aim of improving cancer therapy through EPR-mediated delivery of encapsulated drugs to tumors, thereby reducing toxic side effects to normal tissue. Although some nanoformulations are clinically approved[2], a major clinical breakthrough has not taken place. While tremendous progress has been made in the production of NPs, this has not led to increased NP accumulation in tumors[3]. Furthermore, our fundamental understanding of tumor physiology is still incomplete, which might explain why nanoformulations with excellent pre-clinical results have failed in clinical trials.

To advance efforts to improve NP delivery to solid tumors, the tumor models used in pre-clinical work, which are most often subcutaneous models, must be characterized and better understood and compared to patient tumors. Tumor properties such as vascularity, vascular permeability, cell density, stromal content and interstitial fluid pressure can affect both extravasation and penetration of NPs into the tumor stroma [4–7]. While knowledge of these properties is necessary to understand the barriers faced by macromolecules and NPs, it is equally important to identify *in vivo* methodologies that can predict the efficacy of NP medications in individual patients to know when drug-loaded NPs will be superior to conventional drug formulations. The potential of NPs in solid tumors has been characterized previously by injection of diagnostic NPs labeled either with radioactive positron emission tomography (PET)-tracers or with magnetic resonance imaging (MRI) contrast agents[8–11]. While this approach can provide a macroscopic measure of the uptake of NPs in the entire tumor and in tumor subregions, it offers little insight into the distribution of NPs on a microscopic level. As seen in the present study and in many others[12–15], the distribution

of NPs in the tumor interstitium can be extremely heterogeneous, making overall NP uptake a poor predictor of therapeutic effect.

In the present study, 5 human tumor xenograft models with different vascularization, stroma and cellularity were used to investigate how these characteristics affect NP accumulation. We compared relevant imaging modalities including micro-computed tomography (μCT), contrast enhanced ultrasound (CEUS), diffusion weighted MRI (DW-MRI), dynamic contrast enhanced MRI (DCE-MRI) and fluorescence microscopy. Together these techniques provide complementary information on tumor vascularity and stromal content and enabled us to assess their impact on NP uptake and distribution. Thus, in this multimodality imaging study, we describe the vascular and stromal characteristics of five diverse tumor models and correlate these features to NP tumor uptake. In addition we highlight some of the challenges and limitations of these tumor models and imaging modalities.

Material and Methods

Cell lines and inoculation

The tumors investigated covered a variation in vascular, cellular and collagen densities, and included two prostate carcinoma cell lines, PC3 and PC3/2G7[16], a triple negative breast cancer cell line, MDA-MB-231, an epidermoid carcinoma, A431, and osteosarcoma, OHS[17], all human cell lines.

Tumor cell lines were cultured in the following media supplemented with 10% fetal bovine serum (FBS, Sigma-Aldrich); MDA-MB-231 and OHS in Roswell Park Memorial Institute (RPMI) 1640 Medium (Gibco ThermoFisher, 21875-034), PC3, PC3/2G7 and A431 in Dulbecco's modified eagles medium (DMEM). Cells were maintained at 37°C and 5% CO_2 in exponential growth phase until they were detached by trypsin, resuspended in cell medium containing 1% v/v penicillin/streptomycin (Sigma-Aldrich) and kept on ice until implantation.

Animal handling

Female Balb/c nude mice were purchased from Harlan at 8 weeks of age and housed in specific pathogen free conditions at 22–23 °C, 50–60% relative humidity. The mice had free access to food and sterile water. All experimental procedures were approved by the *Norwegian Animal Research Authorities.* Before inoculating tumor cells, animals were anesthetized using isoflurane. 3×10^6 cells in 50 μl cell medium were injected subcutaneously on the hind leg, a total of 55 animals were used. Animals were weighed and tumor sizes measured using calipers 2–3 times a week. Tumor volumes were calculated as an ellipsoid $\pi*l*w^2/6$ where l and w are the longest and shortest diameter of the tumor, respectively. Experiments were started when the tumors reached 8–12 mm along the longest axis. Prior to the interventions described below, animals were anesthetized by a subcutaneous injection of fentanyl (0.05 mg/kg, Actavis Group), medetomidine (0.5 mg/kg, Orion Pharma), midazolam (5 mg/kg, Accord Healthcare Limited), /water (2:1:2:5) at a dose of 0.1 ml per 10 g. After treatment, an antidote for sedation and anesthesia (atipamezole (2.5

mg/kg, Orion Pharma) and flumazenil (0.5 mg/kg, Fresenius Kab), water (1:1:8) was injected subcutaneously at the same dose to awaken the mouse.

US-imaging

CEUS imaging of the tumors was performed using the animal scanner Vevo2100 (FUJIFILM VisualSonics, Inc., Toronto, Canada) in non-linear contrast mode at 18 MHz (probe MS250) with a transmit power of 10 %. Image acquisition settings were kept constant for all recordings. From the moment of injection of 50 μl Micromarker™ (as recommended by manufacturer, VisualSonics/Bracco), 260 frames were recorded at 10 frames per sec. This is the maximum number of frames that can be recorded continuously at this rate. Time intensity curves were generated using VisualSonics software on the 2D field of view. A region of interest (ROI) was manually drawn around the tumor and the total intensity in the ROI was measured as a function of time. To subtract the background signal, values from a pre-scan before injection of microbubbles was used. The time intensity curve showed a rapid signal increase until reaching maximum signal intensity, which was defined as the inflow time. Similarly, the time from maximum intensity until the signal dropped below 80 % of the maximum was defined as the outflow time. 80 % was chosen because this was the lowest value most tumors dropped below within the 26 seconds possible for video recording. Inflow time was chosen rather than inflow rate because inflow rate could be more sensitive to field of view in the tumor, amount of contrast agent injected and to tumor size.

μCT

After i.v. injection of 100 μl of ExiTron nano 12000 intravascular contrast agent (Miltenyi Biotec), contrast enhanced μCT images were acquired on a Skyscan 1176 *in vivo* μCT scanner (Bruker microCT) using the following scan parameters: source voltage = 50 kV, tube current = 500 μA, 0.5 mm Al filter, exposure = 252 ms, rotation step = 0.4°, 360° rotation, isotropic resolution = 18 μm. Images were reconstructed using a modified Feldkamp filtered back-projection algorithm. CT image processing was performed in Fiji[18]. 3D tumor ROIs were manually defined, and enhanced blood vessels were segmented from the reconstructed images by applying a multiscale Hessian-based filter[19] followed by a manually defined threshold. The vascular fraction (relative blood volume) was calculated by dividing the vascular volume by the tumor ROI volume, and local vessel diameters were computed using the Local Thickness routine.

MRI

In vivo MRI was performed at 7 Tesla on a Bruker Biospec 70/20 Avance III (Bruker Biospin) with a 86 mm volume resonator for RF transmission and a 4 channel phased array mouse brain surface coil for reception. The mice were anesthetized with Fentanyl/ Medetomidin/Midazolam and the body temperature was maintained at 37°C using warm air. Both respiration rate and temperature were monitored during scanning.

15 contiguous transverse slices with a field of view = 19.2 × 19.2 mm^2, slice thickness = 0.7 mm and interslice distance = 1 mm were acquired for all MRI sequences.

Anatomical MRI—Anatomical 3D images were acquired using a high resolution T2-weighted rapid acquisition with relaxation enhancement (RARE) spin echo (SE) sequence with effective echo time (TE_{eff}) = 50 ms, repetition time (TR) = 2200 ms, RARE factor = 12, number of averages (NA) = 8 and matrix size (MTX) = 192 × 192. 3D tumor ROIs were drawn manually in these high-resolution images and downsampled to match the resolution of DW and DCE images.

DW-MRI—DW images were acquired using a fat-suppressed Stejskal-Tanner prepared spin-echo sequence with echo-planar imaging readout: TE= 25 ms, TR= 2500 ms, 2 segments, NA= 2, MTX = 96 × 96, b-values = 100, 150, 200, 250, 350, 500, 700, 1000 s/mm^2, diffusion gradient separation time = 14ms, diffusion gradient duration = 4 ms and six directions. Due to spatial displacement in the images for some b-values and gradient directions, all DW-images were registered to the b0 images using an affine registration. This was followed by averaging the images over the six directions. Afterwards, the data were fitted voxel wise within the tumor in MATLAB (MathWorks, Natick, MA, USA) using a monoexponential fit yielding the apparent diffusion coefficient (ADC). The median ADC was calculated for the tumor rim, which was defined as the outer 1mm.

DCE-MRI—Pre-contrast T1 maps were computed voxel wise after acquiring a series of images with varying TR using a RARE SE sequence with TE = 6 ms, TR = 5500, 3000, 1500, 800, 400, 300, 260, 230, 200, 170 ms, RARE factor =2, MTX = 64×64. This was followed by dynamic imaging, where a series of 160 T1 weighted images was acquired using a RARE SE sequence with TE=5 ms, TR = 300 ms, RARE factor = 4, MTX = 64×64. After 13 or 14 baseline scans a bolus dose of 0.3 mmol/kg gadodiamide (Omniscan, GE Healthcare) diluted in saline was administered into the catheterized tail vein.

For every tumor the fraction of voxels enhanced by at least 50% within the first minute after contrast agent injection (FEV) was computed from the dynamic scans. In addition, the volume transfer constant (K^{trans}) and the extravascular extracellular space per unit volume of tissue (v_e) and perfusion fraction (v_p) were computed using the extended Tofts model[20]. Voxels with a relative signal increase below 50% and/or an area under the enhancement curve below 0 for the first minute were excluded from the Tofts modelling because slowly or non-enhancing voxels do not fulfill the conditions for two-compartment modelling[20]. The pre-contrast T1 maps were used to convert the signal-intensity-time curves from the DCE-images to contrast-agent-time curves for each voxel as described by Jensen et al[21]. Assuming a two-compartment model[22] and a population based bi-exponential input function[23], K^{trans}, v_e and v_p were estimated voxel-wise by curve fitting in MATLAB.

Nanoparticles—Stabile, bright fluorescent NPs with no leakage of dye was used. NPs (yellow-green carboxylated 100 nm fluospheres, Life Technologies) were characterized for size and zeta potential using dynamic light scattering (DLS, Zetasizer Nano ZS, Malvern). The NPs were diluted in 1x PBS and a total of 0.2 mg NPs were injected as a 100 µl bolus through the tail vein. 24 hours after the injection of NPs, the animals were euthanized by cervical dislocation under anesthesia and the tumors harvested for sectioning.

Labelling endothelial cells—100 μl of Texas Red® labeled Lycopersicon Ensculentum (Tomato) Lectin (1mg/ml, Vector Laboratories) was injected through the tail vein 5 minutes before the animals were euthanized to visualize functional blood vessels.

Sectioning of tumors—After the tumors were removed from the leg of the mouse, each tumor was cut in two along the axis perpendicular to the thighbone. One half was embedded in Tissue Tek®(Sakura Finatek) and frozen in liquid nitrogen, the other half was fixed in formalin and embedded in paraffin. The frozen part of the tumor was sectioned in 25 μm thick sections from three areas spread through the tumor. Prior to microscopy, the sections were mounted on glass slides with a drop of Vectashield Antifade mounting medium with DAPI to label nuclei. The paraffin embedded part of the tumor was sliced in 4 μm thick sections and stained with hematoxylin, erythrosin and saffron (HES).

Microscopy Imaging

Images of entire tumor sections were acquired in 2D on an EVOS FL Auto microscope using specific filtercubes for DAPI, GFP and Texas Red (Life Technologies) and a 20x/0.4 magnification air objective. Three 25 μm frozen sections, from areas spread throughout the tumor, were imaged and analyzed for each tumor and averaged to give the quantity of NPs and functional blood vessels from each tumor. Each section contained 30–100 images depending on tumor size.

Cell nuclei were quantified in 8 images from random locations in each tumor. Number of nuclei and area fraction were measured using ImageJ. The images were automatically thresholded using the “default” threshold algorithm and watershed to separate neighboring nuclei. Nuclei were then counted and the total area summarized using the “analyze particle” function in ImageJ. Presented numbers are the nuclei area fraction (area of nuclei/total area).

In order to quantify blood vessel density and accumulation of NPs, the images were split into the different channels and separated into periphery and center of the section. The periphery was defined as a 1mm broad region along the border of the section. The blood vessel channel was thresholded to a minimum intensity of 25/255 to remove autofluorescence. The resulting images were filtered using a Gaussian filter to remove noise and analyzed with the analyze particle function. The NP channel was thresholded using the “Intermodes” algorithm and counted in the analyze particle function. Numbers reported are the fraction of pixels in the tumor section with signal above threshold.

The amount of fibrillar collagen was evaluated in a subset of the tumors (2 tumors from each type). Fibrillar collagen in frozen sections was imaged by the second harmonic generation (SHG) signal, where two photons are combined in a non-linear process and the emitted signal detected at exactly half the wavelength of the two incident photons. The SHG measurements were performed using the Leica SP8 confocal microscope with a 20x/0.75 water objective. The tumor sections were illuminated by a two-photon laser at 890 nm, and the emitted signal detected at 445±10 nm in the backscattered direction. Images were randomly acquired from the periphery (6–8 images/tumor section, 3 sections/tumor) and from the central part (2–3 images/section, 3 sections/tumor). The images were manually

thresholded to remove background in ImageJ and the analyze particles macro was used to measure the area fraction occupied by collagen fibers.

Animal inclusion

Not all imaging modalities were performed in all animals and some animals were removed from analysis most often due to uncertainty regarding the injection of contrast agent. In table 1, the number of animals included in the different parts of the experiment is listed.

Statistics

Statistical analysis was performed in SPSS Statistics 23.0. Groups were compared with one-way ANOVA with Bonferroni post hoc test. For correlation analysis linear regression or Spearman rank correlation coefficient was used.

Results

Nanoparticles

The polystyrene NPs were characterized with DLS and had a Z-average diameter of 119 nm, a polydispersity index (PDI) of 0.06 and a ζ-potential of −49.6 mV.

Tumor growth

The growth rate of the five subcutaneous tumor models differed (Figure 1). PC3 and MDA-MB-231 tumors showed slow, continuous growth, PC3 reached 300 mm^3 after 30 days. For MDA-MB-231 the tumor take rate was very low, tumors developed in only 3 of 7 animals and reaching 75–100 mm^3 after approximately 55 days. Due to the poor growth, this tumor group contains only 2–3 mice. PC3/2G7 tumors grew slowly initially but tumor growth increased exponentially after reaching a volume of around 300 mm^3 at day 17–20. A431 tumors showed rapid, continuous growth and the volume was approximately 300 mm^3 after 18 days. OHS tumors showed rapid growth after an initial lag phase of 10–12 days resulting in tumors around 300 mm^3 after 25 days.

Histology

Histopathological features of each tumor were assessed using HES-stained sections (Figure 2). Both prostate carcinoma models (PC3 and PC3/2G7) and the breast cancer model (MDA-MB-231) were relatively homogeneous in viable, cell-dense regions. Necrotic areas were found in all tumors from these three models. This is consistent with the small number of blood vessels found inside the tumors (Figure 3). The epithelial cell cancer model (A431) had cells with varying degrees of differentiation and with large keratinized and avascular areas. Large necrotic areas in the A431 tumors could be identified as blank regions where the cells were washed away. The osteosarcoma model (OHS) deviated from the carcinomas in several ways. While the carcinomas developed as a solid mass of cells, the OHS tumors were soft and hemorrhagic with a sponge-like appearance. A dense network of blood vessels could be seen throughout the tumors, with extensive connective tissue but no large necrotic areas. Micronecrotic areas due to thrombosis and in sclerotic areas were frequently observed.

μCT

The 3D structure of the tumor vasculature was visualized using *in vivo* contrast enhanced μCT (Figure 3). For all four carcinoma models, the blood vessels were mainly located in the periphery, whereas for the OHS sarcoma model, blood vessels were found throughout the tumor. The percentage of blood vessels was quantified and found to be approximately 0.25% for PC3, 0.5% for PC3/2G7 and MDA-MB-231, 0.8% for A431 and 1.6% for OHS averaged over the entire tumor (Figure 3C). When only the periphery (outer 1 mm) of the tumor was analyzed (Figure 3D) the vascular fraction was twice as high for the carcinomas, and PC3/2G7 showed higher vascular fraction than PC3, consistent with[16]. The relative locations of the blood vessels from the periphery to the center are shown in Figure 3E. The distribution of vessel diameters was found to be in the range of 50–150 μm and relatively similar in the 5 models (Figure 3F).

Dynamic contrast enhanced ultrasound

US imaging is a relatively simple technique with high temporal resolution compared to e.g. MRI and CT. Perfusion was studied by imaging the circulation of microbubbles in the tumor vessels after intravenous injection (Figure 4). In the carcinoma models, increased signal intensity was mainly observed in the periphery of the tumors, whereas the signal intensity increased throughout the whole osteosarcoma model. The inflow time and outflow time correlated, i.e., the tumors with rapid inflow times also showed rapid signal decay (Spearman's correlation = 0.54, $p = 0.005$). However, because of limitations of the ultrasound imaging system (i.e maximum recording time of 26 seconds at 10 frames/second), multiple tumors had to bee excluded from the analysis due to too long outflow time. PC3 and MDA-MB-231 tumors displayed more rapid inflow as well as clearance compared to the other three tumor models. PC3/27 and A431 had similar inflow times about 5 seconds while OHS had longer and more variable inflow times. The outflow time of these three models where similar and around 10–15 seconds.

Dynamic contrast enhanced MRI

DCE-MRI provides insights into the perfusion of the tumor and leakiness of the blood vessels (Figure 5). We defined the fraction of enhanced voxels (FEV) as the fraction of voxel with >50% signal increase within the first minute after injection of gadolinium, which excludes necrotic and poorly vascularized regions. Figure 5A–E shows T2-images of the tumors (left) and post contrast T1-images (right). FEV differed significantly ($p = 0.011$, one-way ANOVA), but was found to correlate significantly ($p = 0.005$) with the size of the tumor as larger tumors had lower FEV (Figure 10B). The shapes of the relative signal intensity (RSI) time curves for enhancing voxels have previously been used to describe the aggressiveness of tumors[24, 25] and are shown in Figure 5F. The RSI curve-shapes show that PC3 has a slow, continuous enhancement pattern (benign/least aggressive), PC3/2G7 and A431 have a plateau pattern, and MDA-MB-231 and OHS have a rapid enhancement and washout pattern (malignant/most aggressive). Interestingly, MDA-MB-231 had slow growth and relatively low tumor take showing that "aggressivity" of a tumor model has many facets.

K^{trans} depends both on the blood flow and the vessel permeability - surface area product and describes the transport of the low molecular weight gadolinium-based contrast agent from the intravascular to extravascular space. We estimated K^{trans} only for enhancing voxels, and K^{trans} was relatively similar for all tumors (Figure 5H).

Diffusion-weighted MRI

DW-MRI can potentially characterize different compartments in the tumors through different diffusion weighting and has the advantage that no contrast agent is needed. In all four carcinomas, the histology (Figure 2) showed large necrotic areas, primarily in the central part of the tumor. Thus, the diffusivity and perfusion fraction were determined only in the tumor periphery, which was defined as the outer 1 mm. Figure 5I shows that the intra-group variation in mean diffusivity was relatively small compared to the inter-group variation and all tumor models were significantly different to each other ($p<0.015$, one-way ANOVA, LSD post hoc test).

Fluorescence and multiphoton microscopy

After completing the *in vivo* imaging, NPs were injected and allowed to circulate for 24 hours to observe stabile NP accumulation in the tumor interstitium. The accumulation of NPs and blood vessel-, cell-, and collagen density were determined by their area fractions in the tumor sections.

All tumor models showed the presence of NPs, but their distribution was highly heterogeneous and they were generally located close to blood vessels. Most tumors displayed large areas without NPs. Representative images from the 5 models are shown in Figure 6. On average, PC3/2G7, A431 and OHS tumors accumulated the most NPs, but the variation between the tumors of the same type was large. PC3, PC3/2G7 and A431 trended towards more NPs in the outer 1mm (Figure 7A–C), with approximately 2x higher median NP/area in the periphery.

Blood vessel density had a high intra-group variation, comparable to the intergroup variation (Figure 7D, E). Consistent with uCT and MRI, the OHS had highest blood vessel density in the tumor core (Figure 7E). Blood vessel density showed a positive correlation with NP accumulation (Figure 9A).

The area fraction representing cell nuclei density was 0.15–0.3 (Figure 7F) with a highly significant variation between the five tumor models ($p < 0.0001$, one way ANOVA). However, cell density did not seem to affect NP uptake (Figure 9D). Collagen (Figure 8) was imaged in a subset of the tumors and found to be highly variable, with local collagen densities ranging from zero to more than 10%. A431 was by far the least collagen-rich tumor with significantly less collagen than all other groups (one-way ANOVA). Notably, PC3 tumors had significantly higher density of collagen than PC3/2G7 tumors ($p=0.007$ center and 0.026 periphery, t-test). There was no correlation between NP uptake and collagen density although the lowest NP accumulation were found in tumors with highest collagen density (Figure 9J).

Imaging method comparisons and correlations

NP accumulation in tumors is a complex phenomenon. Linear regression analysis and Spearman Rank correlation were performed to investigate the correlation between NP accumulation and the measured tumor properties. In Figure 9A it can be seen that blood vessel density had significant linear correlation with NP accumulation. The same relation was not found for the periphery alone (Figure 9B). Interestingly, it was found that the inflow of microbubbles weakly correlated with NP accumulation ($p=0.041$, Spearman correlation, Figure 9C), and also US outflow indicated the same trend (not shown). No correlation was found between MRI- and CT-derived parameters and NP accumulation. It should be noted that the group sizes comparing CT to NP accumulation was lower than for the other modalities.

Figure 10 shows correlation between some of the characteristic tumor parameters apart from NP accumulation. The cell density (based on nuclei area fraction) had a significant negative linear correlation with the ADC (Figure 10A). Figure 10B shows that the fraction of enhancing voxels is significantly inversely correlated with tumor size indicating that as tumors grow larger, they are unable to keep the whole tumor perfused, which is also confirmed by the necrosis found in the carcinomas. Interestingly, OHS does not deviate from this correlation. In Figure 10C it can be seen that the extracellular - extravascular compartment measured by DCE-MRI correlates with ADC by spearman rank correlation and in Figure 10D it is shown that perfusion fraction measured by DCE-MRI correlated linearly with FBV from μCT. These relations are expected, but importantly indicate that the variations seen are results of true biological variations and not of random noise in the measurements. Although the tumor models exhibited variation, some generalizations have been suggested in table 2.

Discussion

Characterization of human tumor xenografts and nanoparticle accumulation

Successful delivery of NPs to a solid tumor requires that the tumor is well vascularized and that the NPs can extravasate and penetrate throughout the tumor interstitium. Knowledge about tumor vascular density, morphology and permeability, the tumor interstitium and the impact of these parameters on NP accumulation is therefore highly important. Our characterization of 5 different tumor models showed that NP accumulation correlated with vascular density measured by fluorescence microscopy as well as the inflow of microbubbles. The latter is of particular interest and demonstrates that vessel morphology and perfusion also are important parameters for NP accumulation.

Though much effort is put into the optimization of NP sizes and surface coatings to improve NP accumulation in tumors[26], a recent review indicated that the last decade of NP development has not resulted in improvements in this regard[3]. In our study we used monodisperse polystyrene NPs stabilized by a highly negative ζ-potential caused by acid groups on the surface. These commercial NPs were previously used in comparable studies[4, 27–29], and although modifications such as PEGylation of these NPs[30] would increase circulation time and tumor accumulation, using commercial NPs is a step towards

standardization of evaluation systems and facilitates more direct lab-to-lab comparisons[14]. We have also observed in other experiments that the differences in accumulation of these commercial NPs in PC3 and OHS tumors are comparable to our in-house poly (alkyl cyanoacrylate) NPs (unpublished data).

Angiogenesis is a hallmark of cancer[31] and functional vascularization is important for efficient NP delivery to the tumor[32]. We studied the vasculature using multiple imaging modalities to get a detailed understanding of the vascular characteristics of the tumor models. All four carcinoma models showed varying degrees of vascularization in the periphery, whereas avascular and necrotic areas were observed in the central part of the tumors, which is also seen in aggressive tumors in patients[33]. Imaging of NP distribution showed that these central areas were inaccessible to NPs, and cells surviving in these areas would probably remain unaffected by drugs carried by NPs. In the OHS sarcoma model on the other hand, blood vessels and NPs were observed throughout the tumor, and very little necrosis was seen. The vascular densities in the tumor periphery were in accordance with previous studies where PC3/2G7 was reported to have higher density than PC3[16]. A431 has also been reported to have relatively high blood vessel density[34], but was found to have a very chaotic interior with islands of cell-dense areas, necrotic areas and keratinized areas, which have previously been shown to severely limit NP accumulation[35].

Hyperpermeable tumor blood vessels are the main rationale behind the development of nanomedicine. However, the EPR effect is highly heterogeneous[36], and sarcomas are, as confirmed in this study, reported to have limited EPR effect compared to carcinomas[8]. K^{trans} from DCE-MRI is often used to characterize vessel leakiness to MRI contrast agents and has been shown to be high in tumors[37]. In our study, we found no direct correlation between K^{trans} and NP accumulation. Vascular surface area and perfusion can be the determining factors in K^{trans} measurements[38], so K^{trans} is not always an unambiguous parameter for vessel leakiness. Furthermore, extravasation of the low molecular weight contrast agent gadodiamide may not accurately reflect extravasation of larger NPs which has also been shown previously[39] and calculations based on larger NPs such as iron oxide NPs might be more clinical relevant as also observed by others[39, 40].

Inflow time of microbubbles from the tumor was found to be a predictor of NP accumulation. As the microbubbles have a size from 2–4um, they are constrained to the vascular space, therefore a long transit time is not caused by extravasation but rather reflects the morphology of the vasculature. The retention of microbubbles is thus probably due to chaotic microvasculature having high vascular resistance with shunts and dead ends[36], preventing effective flow. The correlation between inflow time for microbubbles and NP accumulation could indicate that not only blood vessel fenestrae, but also vascular morphology and long transit times are important factors that facilitate NP extravasation. US contrast agent in- or outflow rates did not correlate with vascular density (not shown in a separate graph).

The tumor interstitium consists of a network of collagen fibers embedded in a hydrophilic gel of glycosaminoglycans and constitutes a barrier for delivery of NPs[7, 41]. The high interstitial fluid pressure and tortuous interstitium in tumors limit the penetration of NPs

throughout the interstitium[42]. Densities of cells and collagen could be important, both for NP extravasation and especially for transport away from the vessels. However, neither factors correlated with NP accumulation in our study although tumors with high collagen content showed low NP accumulation. From DW-MRI, it was found that A431 tumors had the highest diffusivity, correlating with the lowest cell and collagen density, but not entirely surprising; high water diffusivity did not result in high NP accumulation.

As this study also aimed to characterize different tumor models for future research, one important question is whether subcutaneous human tumor xenografts have an artificially high EPR compared to patient tumors. Regarding the accumulation of NPs, the few studies carried out in patients indicate that EPR is a very heterogeneous parameter in human tumors[43–45]. The K^{trans} measured in our tumor models (0.02–0.2 min^{-1}), is within the range measured in solid tumors in patients[46]. Blood vessel density is not often reported in human tumors, but the range of 1–3 % that we measured in the non-necrotic tumor regions is similar to reports from patients[47]. In consistency with our results, carcinomas in patients are reported to have the higher vascular density in the tumor periphery compared to central part of the tumor[48].

Preselection of patients and personalized treatment are key factors to achieve successful clinical trials with nanomedicine. This is reported both in a recent review[49] and experimentally [10, 11, 50]. It is a clear benefit to the patients and to the society to be able to predict the success of nanomedicines and to be able to optimize and personalize the treatment. There is a growing understanding that the EPR effect is heterogeneous and might be rather limited. This is observed in patients[43, 51] and has been suggested as one of the reasons why exploiting the EPR-effect has been difficult clinically[52]. Thus, there is a need to find parameters to be used for patient selection for nanomedicine. Our results suggest that vascular mapping, both by CEUS and other imaging modalities could be useful in this context. CEUS has the advantage of being a low-cost and easy imaging modality and our findings might be clinical important and will be followed up.

Multimodality tumor imaging

The imaging modalities can provide some of the same information, but variations such as differently sized contrast agents and different spatial and temporal resolution make the imaging techniques complementary and each have its advantages. We used CEUS, μCT and MRI primarily to evaluate the tumor vasculature, but also to identify properties possibly affecting the accumulation of NPs. For CEUS and μCT, the contrast agents are assumed to remain in the blood pool and were used to characterize tumor vascular structure and density. The complementary in the imaging techniques was reflected in the positive correlation between vascular fraction measured by MRI-DCE and μCT both methods measure larger blood vessels, whereas no significant correlation was found between vascular fraction and vessel density measured by fluorescence microscopy which also image smaller vessels.

Other trends found across the various techniques were the presence of avascular regions consistently seen by microscopy, CEUS, CT and DCE MRI in great compliance. Also, the general trend seen with microscopy, CEUS and μCT was that PC3 and MDA-MB-231 tumors had the fewest blood vessels in which corresponded to the least NPs accumulated. It

was found that ADC indeed correlates inversely with cell density and increases with increased extravascular extracellular space (Ve).

US is a simple and available technique. Single microbubbles (3–5 μm) can be imaged in CEUS, thereby obtaining information well beyond the spatial resolution of US imaging. It has previously been shown that CEUS imaging of tumor vasculature could predict the accumulation of 10nm NPs[53]. There are multiple parameters that can be obtained from CEUS imaging[54]. We performed time intensity curve (TIC) analysis and reported the in- and outflow times of microbubbles, with the former correlating significantly with the accumulation of NPs. The temporal information of CEUS imaging may therefore give important information about the functionality of the tumor vasculature. If a tumor consists of a few and mainly large vessels, it can be expected that the inflow and outflow of bubbles is very rapid and follows the distribution and clearance in blood. However, if the tumor has microvasculature that is chaotic and poorly developed with dead ends, shunts and slow blood flow, as reported for many tumors[55], the bubbles might get stuck in the capillaries and increase the US signal for prolonged periods. Interestingly, as some OHS tumors have similar in- and outflow times as A431 and PC3/2G7 tumors, this indicates that TIC measurements are not only sensitive to vessel density. This indicates that CEUS can give insight into the blood vessel morphology and function rather than the quantity. Consistently, the PC3/2G7 model which has relatively long transit time of microbubbles, also has poorly developed and immature vasculature compared to PC3 with lower pericyte coverage of blood vessels[16].

Contrast enhanced μCT is an established method for 3D visualization of the vascular structure of tumors and has been used previously for thorough characterization of the vasculature in multiple tumor models, including A431[34]. While the theoretical resolution of our system was 18μm, the actual detection limit was around 40 μm due to a low contrast to noise ratio. Thus imaging capillaries, which might be the most critical vessel in terms of NP delivery and EPR, was difficult. This challenge for *in vivo* μCT has been noted also by others[34]. However, μCT allows for 3D reconstruction and calculations of both blood volume and vessel diameters from the entire tumor.

Clinically relevant DCE-MRI contrast agents, such as the one used in this study, are low molecular weight gadolinium chelates that leak out of hyperpermeable tumor blood vessels and has in previous work been used to classify tumor models as EPR-positive or negative[39]. Extravasation of the contrast agent from the blood to the extracellular extravascular space can be characterized by the parameter K^{trans}. However, it is challenging to differentiate between “few and very leaky” and “many and less leaky” blood vessels. Also, since most NPs are much larger than the gadolinium chelates, K^{trans} might not be representative for NP accumulation, as was observed in this study.

DW-MRI has the advantage of being non-invasive and holds significant potential for characterizing tissue microstructure. By acquiring images with multiple b-values, one can in principle model both the water displacement arising from blood flow and water diffusion in the extravascular space[56]. However, fitting methods are highly sensitive to noise, which is a problem especially at high b-values. In necrotic tissue, both high water content and high

diffusivity can be expected, and the signal from these areas can skew the average diffusivity of the entire tumor. In our study, we chose to include only the outer three voxels of the tumor ROI in order to include the vascular (and NP-accumulating) parts of the tumor. The reported diffusivity will depend on all barriers restricting diffusion of water such as cells and surrounding connective tissue, which is in compliance with our observations.

This study shows that vascular density and vascular morphology can predict uptake of NPs in tumors. However a limitation is that the study cannot conclude regarding the EPR effect as the accumulation is only reported at one timepoint. An interesting follow up would be to use various infrared labelled NPs and iron oxide NPs and measure the EPR effect by small animal optical imaging and MRI. Also, the correlation between NP accumulation and the flow of microbubbles through the tumor should be followed up with more comprehensive animal groups, more clinically relevant NPs and smaller, less necrotic tumors.

Conclusion

Nanotechnology has made it possible to make a range of interesting NPs, however, there is limited understanding of the EPR effect and the behavior of NPs in tumor tissue. This might be one of the reasons that drug-loaded NPs have not achieved the clinical success that was anticipated by the EPR effect. We characterized five tumor xenografts and show that the models have different properties that can be exploited to evaluate NP performance. The tumor vasculature was imaged using multiple modalities, and we found that neither DCE- and, DW-MRI, or μCT could predict NP accumulation, whereas both microscopy of functional blood vessels and time-intensity curve analysis from CEUS correlated with NP accumulation. This indicates that characterization of the tumor vasculature can be a valuable alternative to theranostic or reporter-NP approaches to predicted the therapeutic effect of nanomedicines.

Acknowledgments

This research was supported by Norwegian regional health authority (ES, JK, SS) and NIH grant CA049248 (DJW). Ingunn Nervik at CMIC NTNU and Astrid Bjørkøy at MINT NTNU are acknowledged for sectioning and staining (IN) and collagen imaging (AB). MR Imaging was performed at the MR Core Facility at NTNU.

References

1. Matsumura Y, Maeda H. A New Concept for Macromolecular Therapeutics in Cancer-Chemotherapy - Mechanism of Tumoritropic Accumulation of Proteins and the Antitumor Agent Smancs. Cancer Res. 1986; 46:6387–6392. [PubMed: 2946403]
2. Wicki A, Witzigmann D, Balasubramanian V, Huwyler J. Nanomedicine in cancer therapy: Challenges, opportunities, and clinical applications. J Controlled Release. 2015; 200:138–157.
3. Wilhelm S, Tavares AJ, Dai Q, Ohta S, Audet J, Dvorak HF, Chan WCW. Analysis of nanoparticle delivery to tumours. Nat Rev Mater. 2016; 1
4. Torosean S, Flynn B, Axelsson J, Gunn J, Samkoe KS, Hasan T, Doyley MM, Pogue BW. Nanoparticle uptake in tumors is mediated by the interplay of vascular and collagen density with interstitial pressure. Nanomed-Nanotechnol. 2013; 9:151–158.
5. Ekdawi SN, Jaffray DA, Allen C. Nanomedicine and tumor heterogeneity: Concept and complex reality. Nano Today. 2016; 11:402–414.
6. Chauhan VP, Stylianopoulos T, Boucher Y, Jain RK. Delivery of Molecular and Nanoscale Medicine to Tumors: Transport Barriers and Strategies. Annu Rev Chem Biomol. 2011; 2:281–298.

7. Eikenes L, Tari M, Tufto I, Bruland OS, Davies CD. Hyaluronidase induces a transcapillary pressure gradient and improves the distribution and uptake of liposomal doxorubicin (Caelyx (TM)) in human osteosarcoma xenografts. Brit J Cancer. 2005; 93:81–88. [PubMed: 15942637]
8. Hansen AE, Petersen AL, Henriksen JR, Boerresen B, Rasmussen P, Elema DR, Rosenschold PM, Kristensen AT, Kjaer A, Andresen TL. Positron Emission Tomography Based Elucidation of the Enhanced Permeability and Retention Effect in Dogs with Cancer Using Copper-64 Liposomes. Acs Nano. 2015; 9:6985–6995. [PubMed: 26022907]
9. Kiessling F, Mertens ME, Grimm J, Lammers T. Nanoparticles for imaging: top or flop? Radiology. 2014; 273:10–28. [PubMed: 25247562]
10. Lee H, Shields AF, Siegel BA, Miller KD, Krop I, Ma CX, LoRusso PM, Munster PN, Campbell K, Gaddy DF, Leonard SC, Geretti E, Blocker SJ, Kirpotin DB, Moyo V, Wickham TJ, Hendriks BS. Cu-64-MM-302 Positron Emission Tomography Quantifies Variability of Enhanced Permeability and Retention of Nanoparticles in Relation to Treatment Response in Patients with Metastatic Breast Cancer. Clin Cancer Res. 2017; 23:4190–4202. [PubMed: 28298546]
11. Miller MA, Gadde S, Pfirschke C, Engblom C, Sprachman MM, Kohler RH, Yang KS, Laughney AM, Wojtkiewicz G, Kamaly N, Bhonagiri S, Pittet MJ, Farokhzad OC, Weissleder R. Predicting therapeutic nanomedicine efficacy using a companion magnetic resonance imaging nanoparticle. Sci Transl Med. 2015; 7
12. Ekdawi SN, Stewart JMP, Dunne M, Stapleton S, Mitsakakis N, Dou YN, Jaffray DA, Allen C. Spatial and temporal mapping of heterogeneity in liposome uptake and microvascular distribution in an orthotopic tumor xenograft model. J Controlled Release. 2015; 207:101–111.
13. Miller MA, Zheng YR, Gadde S, Pfirschke C, Zope H, Engblom C, Kohler RH, Iwamoto Y, Yang KS, Askevold B, Kolishetti N, Pittet M, Lippard SJ, Farokhzad OC, Weissleder R. Tumour-associated macrophages act as a slow-release reservoir of nano-therapeutic Pt(IV) pro-drug. Nat Commun. 2015; 6:8692. [PubMed: 26503691]
14. Crommelin DJ, Florence AT. Towards more effective advanced drug delivery systems. Int J Pharm. 2013; 454:496–511. [PubMed: 23415662]
15. Hak S, Cebulla J, Huuse EM, Davies CD, Mulder WJM, Larsson HBW, Haraldseth O. Periodicity in tumor vasculature targeting kinetics of ligand-functionalized nanoparticles studied by dynamic contrast enhanced magnetic resonance imaging and intravital microscopy. Angiogenesis. 2014; 17:93–107. [PubMed: 23982332]
16. Zhang K, Waxman DJ. Impact of tumor vascularity on responsiveness to antiangiogenesis in a prostate cancer stem cell-derived tumor model. Molecular cancer therapeutics. 2013; 12:787–798. [PubMed: 23635653]
17. Fodstad O, Brogger A, Bruland O, Solheim OP, Nesland JM, Pihl A. Characteristics of a Cell-Line Established from a Patient with Multiple Osteosarcoma, Appearing 13 Years after Treatment for Bilateral Retinoblastoma. Int J Cancer. 1986; 38:33–40. [PubMed: 3459716]
18. Schindelin J, Rueden CT, Hiner MC, Eliceiri KW. The ImageJ ecosystem: An open platform for biomedical image analysis. Mol Reprod Dev. 2015; 82:518–529. [PubMed: 26153368]
19. Sato Y, Nakajima S, Atsumi H, Koller T, Gerig G, Yoshida S, Kikinis R. 3D multi-scale line filter for segmentation and visualization of curvilinear structures in medical images. Lect Notes Comput Sc. 1997; 1205:213–222.
20. Tofts PS. Modeling tracer kinetics in dynamic Gd-DTPA MR imaging. Jmri-J Magn Reson Im. 1997; 7:91–101.
21. Jensen LR, Huuse EM, Bathen TF, Goa PE, Bofin AM, Pedersen TB, Lundgren S, Gribbestad IS. Assessment of early docetaxel response in an experimental model of human breast cancer using DCE-MRI, ex vivo HR MAS, and in vivo H-1 MRS. Nmr Biomed. 2010; 23:56–65. [PubMed: 19650073]
22. Tofts PS, Brix G, Buckley DL, Evelhoch JL, Henderson E, Knopp M, Larsson HBW, Lee TY, Mayr NA, Parker GJM, Port RE, Taylor J, Weisskoff RM. Estimating kinetic parameters from dynamic contrast-enhanced T(1)-weighted MRI of a diffusable tracer: Standardized quantities and symbols. J Magn Reson Imaging. 1999; 10:223–232. [PubMed: 10508281]

23. Jensen LR, Berge K, Batheni TF, Wergedah H, Schonberg SA, Bofin A, Berge RK, Gribbestad IS. Effect of dietary tetradecylthioacetic acid on colon cancer growth studied by dynamic contrast enhanced MRI. Cancer Biol Ther. 2007; 6:1810–1816. [PubMed: 18287814]
24. Hayes C, Padhani AR, Leach MO. Assessing changes in tumour vascular function using dynamic contrast-enhanced magnetic resonance imaging. Nmr Biomed. 2002; 15:154–163. [PubMed: 11870911]
25. Daniel BL, Yen YF, Glover GH, Ikeda DM, Birdwell RL, Sawyer-Glover AM, Black JW, Plevritis SK, Jeffrey SS, Herfkens RJ. Breast disease: Dynamic spiral MR imaging. Radiology. 1998; 209:499–509. [PubMed: 9807580]
26. Perrault SD, Walkey C, Jennings T, Fischer HC, Chan WCW. Mediating Tumor Targeting Efficiency of Nanoparticles Through Design. Nano Lett. 2009; 9:1909–1915. [PubMed: 19344179]
27. Na JH, Koo H, Lee S, Min KH, Park K, Yoo H, Lee SH, Park JH, Kwon IC, Jeong SY, Kim K. Real-time and non-invasive optical imaging of tumor-targeting glycol chitosan nanoparticles in various tumor models. Biomaterials. 2011; 32:5252–5261. [PubMed: 21513975]
28. Yaehne K, Tekrony A, Clancy A, Gregoriou Y, Walker J, Dean K, Nguyen T, Doiron A, Rinker K, Jiang XY, Childs S, Cramb D. Nanoparticle Accumulation in Angiogenic Tissues: Towards Predictable Pharmacokinetics. Small. 2013; 9:3118–3127. [PubMed: 23463664]
29. Lee PC, Peng CL, Shieh MJ. Combining the single-walled carbon nanotubes with low voltage electrical stimulation to improve accumulation of nanomedicines in tumor for effective cancer therapy. J Controlled Release. 2016; 225:140–151.
30. De Cock I, Lajoinie G, Versluis M, De Smedt SC, Lentacker I. Sonoprinting and the importance of microbubble loading for the ultrasound mediated cellular delivery of nanoparticles. Biomaterials. 2016; 83:294–307. [PubMed: 26796042]
31. Hanahan D, Weinberg RA. The hallmarks of cancer. Cell. 2000; 100:57–70. [PubMed: 10647931]
32. Stapleton S, Allen C, Pintilie M, Jaffray DA. Tumor perfusion imaging predicts the intra-tumoral accumulation of liposomes. J Controlled Release. 2013; 172:351–357.
33. Shirakawa K, Tsuda H, Heike Y, Kato K, Asada R, Inomata M, Sasaki H, Kasumi F, Yoshimoto M, Iwanaga T, Konishi F, Terada M, Wakasugi H. Absence of endothelial cells, central necrosis, and fibrosis are associated with aggressive inflammatory breast cancer. Cancer Res. 2001; 61:445–451. [PubMed: 11212228]
34. Ehling J, Theek B, Gremse F, Baetke S, Mockel D, Maynard J, Ricketts SA, Grull H, Neeman M, Knuechel R, Lederle W, Kiessling F, Lammers T. Micro-CT imaging of tumor angiogenesis: quantitative measures describing micromorphology and vascularization. The American journal of pathology. 2014; 184:431–441. [PubMed: 24262753]
35. San Martin JAD, Hare JI, Yates JWT, Barry ST. Tumour stromal morphology impacts nanomedicine cytotoxicity in patient-derived xenografts. Nanomed-Nanotechnol. 2015; 11:1247–1252.
36. Jain RK, Stylianopoulos T. Delivering nanomedicine to solid tumors. Nat Rev Clin Oncol. 2010; 7:653–664. [PubMed: 20838415]
37. Turkbey B, Kobayashi H, Ogawa M, Bernardo M, Choyke PL. Imaging of Tumor Angiogenesis: Functional or Targeted? Am J Roentgenol. 2009; 193:304–313. [PubMed: 19620425]
38. Kim E, Kim J, Maelandsmo GM, Johansen B, Moestue SA. Anti-angiogenic therapy affects the relationship between tumor vascular structure and function: A correlation study between micro-computed tomography angiography and dynamic contrast enhanced MRI. Magn Reson Med. 2016
39. Karageorgis A, Dufort S, Sancey L, Henry M, Hirsjarvi S, Passirani C, Benoit JP, Gravier J, Texier I, Montigon O, Benmerad M, Siroux V, Barbier EL, Coll JL. An MRI-based classification scheme to predict passive access of 5 to 50-nm large nanoparticles to tumors. Sci Rep-Uk. 2016; 6
40. Ramanathan RK, Korn RL, Raghunand N, Sachdev JC, Newbold RG, Jameson G, Fetterly GJ, Prey J, Klinz SG, Kim J, Cain J, Hendriks BS, Drummond DC, Bayever E, Fitzgerald JB. Correlation between Ferumoxytol Uptake in Tumor Lesions by MRI and Response to Nanoliposomal Irinotecan in Patients with Advanced Solid Tumors: A Pilot Study. Clin Cancer Res. 2017; 23:3638–3648. [PubMed: 28159813]

41. Boucher Y, Baxter LT, Jain RK. Interstitial Pressure-Gradients in Tissue-Isolated and Subcutaneous Tumors - Implications for Therapy. Cancer Res. 1990; 50:4478–4484. [PubMed: 2369726]

42. Netti PA, Berk DA, Swartz MA, Grodzinsky AJ, Jain RK. Role of extracellular matrix assembly in interstitial transport in solid tumors. Cancer Res. 2000; 60:2497–2503. [PubMed: 10811131]

43. Harrington KJ, Mohammadtaghi S, Uster PS, Glass D, Peters AM, Vile RG, Stewart JS. Effective targeting of solid tumors in patients with locally advanced cancers by radiolabeled pegylated liposomes. Clin Cancer Res. 2001; 7:243–254. [PubMed: 11234875]

44. Koukourakis MI, Koukouraki S, Giatromanolaki A, Archimandritis SC, Skarlatos J, Beroukas K, Bizakis JG, Retalis G, Karkavitsas N, Helidonis ES. Liposomal doxorubicin and conventionally fractionated radiotherapy in the treatment of locally advanced non-small-cell lung cancer and head and neck cancer. J Clin Oncol. 1999; 17:3512–3521. [PubMed: 10550149]

45. Richardson VJ, Ryman BE, Jewkes RF, Jeyasingh K, Tattersall MNH, Newlands ES, Kaye SB. Tissue Distribution and Tumor-Localization of 99m-Technetium-Labeled Liposomes in Cancer-Patients. Brit J Cancer. 1979; 40:35–43. [PubMed: 475960]

46. Liu G, Rugo HS, Wilding G, McShane TM, Evelhoch JL, Ng C, Jackson E, Kelcz F, Yeh BM, Lee FT, Charnsangavej C, Park JW, Ashton EA, Steinfeldt HM, Pithavala YK, Reich SD, Herbst RS. Dynamic contrast-enhanced magnetic resonance imaging as a pharmacodynamic measure of response after acute dosing of AG-013736, an oral angiogenesis inhibitor, in patients with advanced solid tumors: Results from a phase I study. J Clin Oncol. 2005; 23:5464–5473. [PubMed: 16027440]

47. Lissbrant IF, Stattin P, Damber JE, Bergh A. Vascular density is a predictor of cancer-specific survival in prostatic carcinoma. Prostate. 1997; 33:38–45. [PubMed: 9294625]

48. Mattern J, Koomagi R, Volm M. Association of vascular endothelial growth factor expression with intratumoral microvessel density and tumour cell proliferation in human epidermoid lung carcinoma. Brit J Cancer. 1996; 73:931–934. [PubMed: 8611409]

49. Hare JI, Lammers T, Ashford MB, Puri S, Storm G, Barry ST. Challenges and strategies in anti-cancer nanomedicine development: An industry perspective. Advanced Drug Delivery Reviews. 2017; 108:25–38. [PubMed: 27137110]

50. Perez-Medina C, Abdel-Atti D, Tang J, Zhao Y, Fayad ZA, Lewis JS, Mulder WJ, Reiner T. Nanoreporter PET predicts the efficacy of anti-cancer nanotherapy. Nat Commun. 2016; 7:11838. [PubMed: 27319780]

51. Jensen GM, Bunch TH. Conventional liposome performance and evaluation: Lessons from the development of vescan. J Liposome Res. 2007; 17:121–137. [PubMed: 18027233]

52. Nichols JW, Bae YH. EPR: Evidence and fallacy. J Controlled Release. 2014; 190:451–464.

53. Theek B, Gremse F, Kunjachan S, Fokong S, Pola R, Pechar M, Deckers R, Storm G, Ehling J, Kiessling F, Lammers T. Characterizing EPR-mediated passive drug targeting using contrast-enhanced functional ultrasound imaging. J Controlled Release. 2014; 182:83–89.

54. Kong WT, Yuan HX, Cai H, Wang WP, Tang Y, Zhang XL. Early treatment response to sorafenib for rabbit VX2 orthotic liver tumors: evaluation by quantitative contrast-enhanced ultrasound. Tumor Biol. 2015; 36:2593–2599.

55. Pries AR, Hopfner M, le Noble F, Dewhirst MW, Secomb TW. The shunt problem: control of functional shunting in normal and tumour vasculature. Nat Rev Cancer. 2010; 10:587–593. [PubMed: 20631803]

56. Le Bihan D, Breton E, Lallemand D, Aubin ML, Vignaud J, Laval-Jeantet M. Separation of diffusion and perfusion in intravoxel incoherent motion MR imaging. Radiology. 1988; 168:497–505. [PubMed: 3393671]

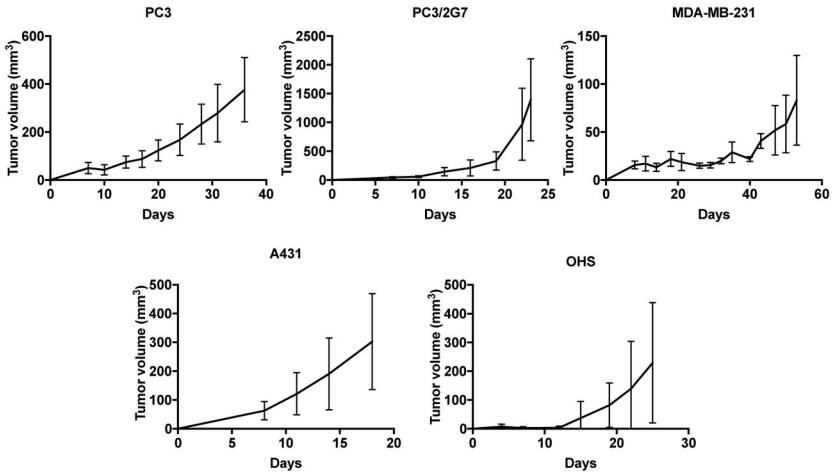

Fig. 1.

Growth rate of the 5 different tumor models. Error bars show standard deviation, PC3: n=7, PC3/2G7: n=7, MDA-MB-231: n=3, A431: n=6 and OHS: n=5.

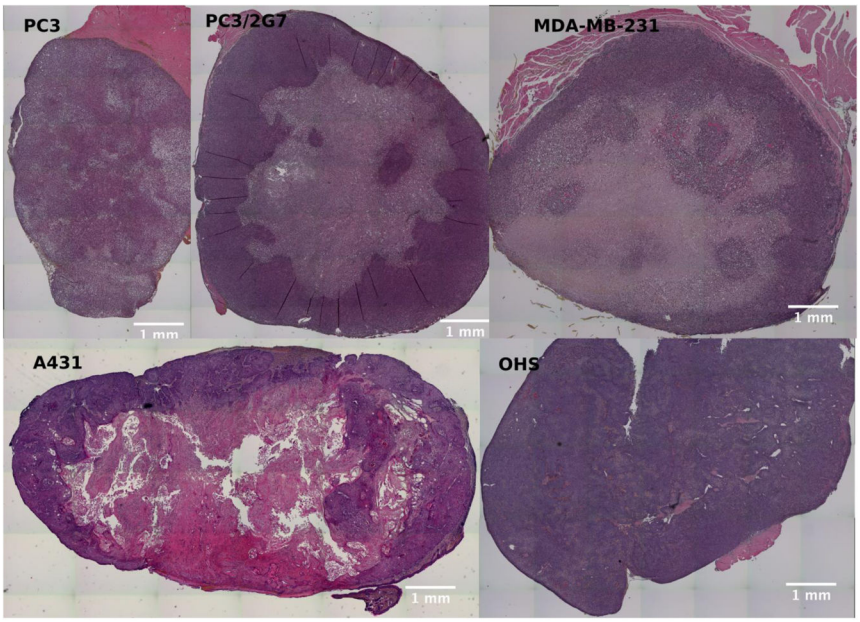

Fig. 2.

HES stained sections of the different tumor models. Necrotic regions are seen either as pale areas or as white regions where dead cells are washed away during preparation.

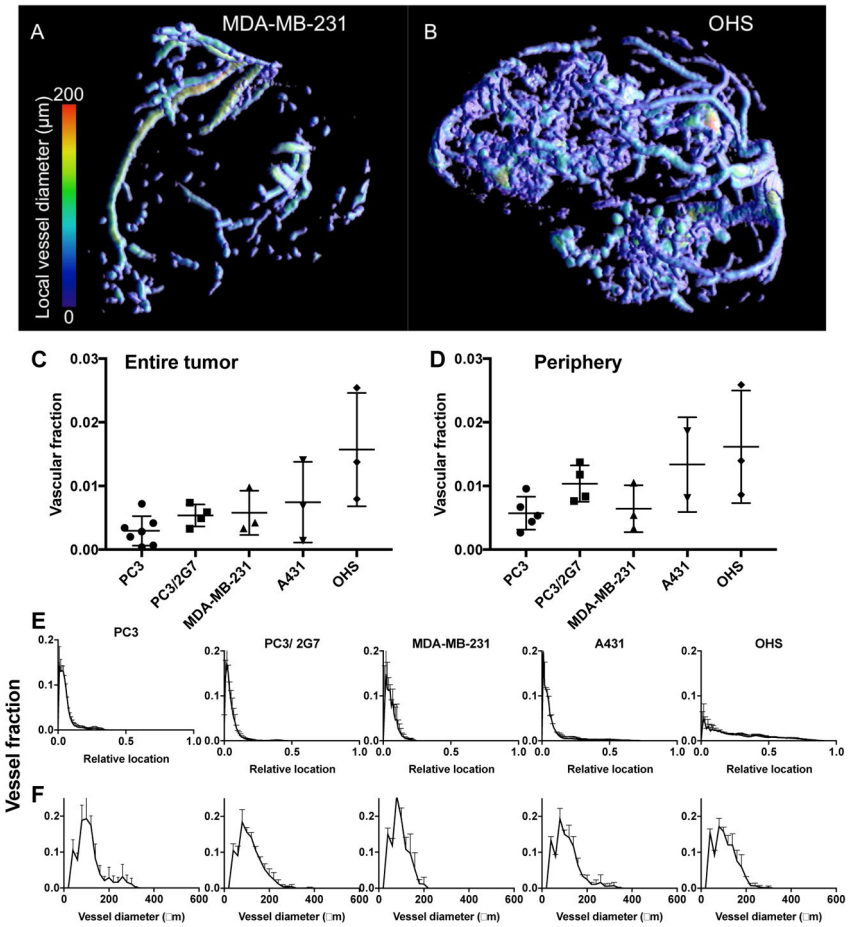

Fig. 3.

In vivo μCT angiography of the tumor models. A and B show 3D renderings of the segmented tumor vasculature from representative MDA-MB-231 and OHS tumors, respectively. C: Vascular fraction of the entire tumor and D: vascular fraction in the rim (outer 1 mm) of the tumors. Each symbol represents one tumor, and the mean and SD are given for each tumor model. E: Distribution of blood vessels from the tumor surface and towards the core. For all tumors except OHS the majority of blood vessels was found in the periphery. F: Distribution of blood vessel diameters.

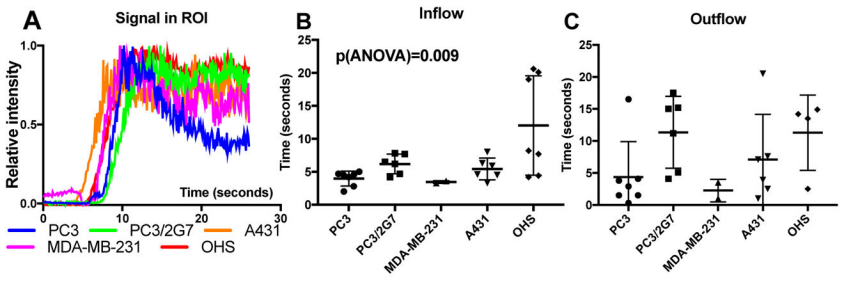

Fig. 4.

CEUS imaging of the 5 different tumor models. A: Representative time-intensity curves for whole tumor ROIs. B: Mean inflow times and C: mean outflow times for the microbubbles. Each symbol represents one tumor, and the mean and SD are given for each tumor model.

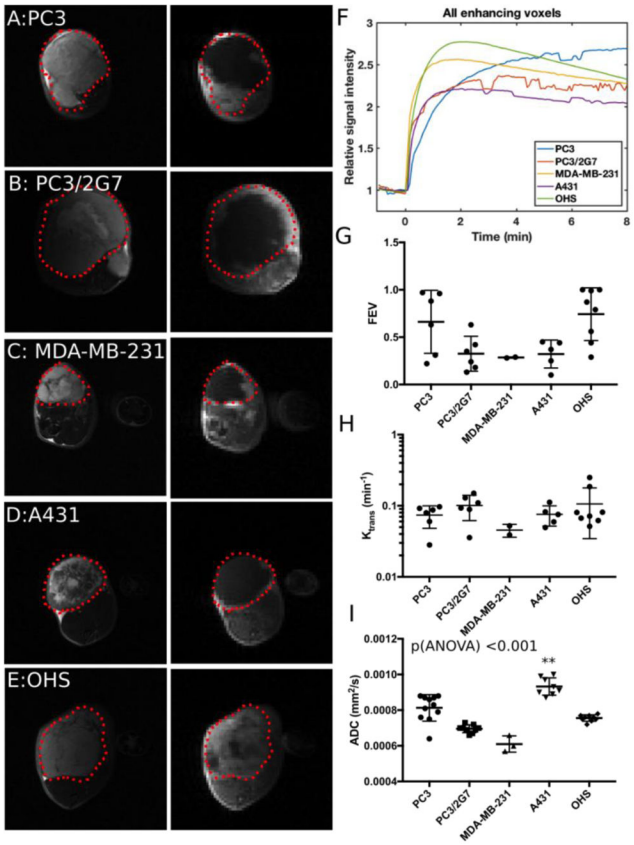

Fig. 5.

MRI data from the 5 tumor models. A–E: T2 weighted images (left) of the tumor outlined in red and T1-weighted image (right) 1 minute after injection of gadolinium contrast agent. Signal enhancement due to presence of the contrast agent can be seen mainly in the periphery of the carcinomas (A–D) and in most of the OHS sarcoma model (E). F: Mean signal enhancement curves for one tumor from each model. G: Fraction of voxels in the tumor that show more than 1.5 RSI after 1 minute. H: Median K^{trans} of the enhancing tumor voxels. I: Median ADC values calculated from diffusion weighted MRI for 1mm thick tumor rim ROI. ** Indicates tumor groups significantly different from the others.

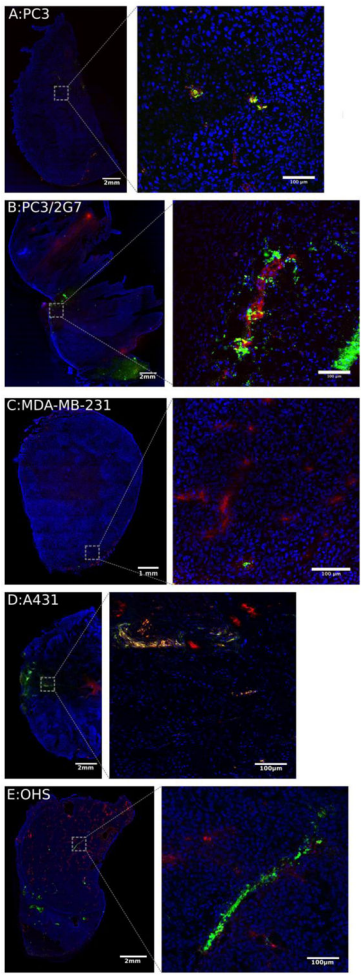

Fig. 6.

Fluorescence imaging of the 5 tumor models. Nuclei are stained blue (DAPI), blood vessels red (Texas red) and NPs green (yellow-green fluospheres). Left images show the entire tumor sections, right images are confocal images of selected areas.

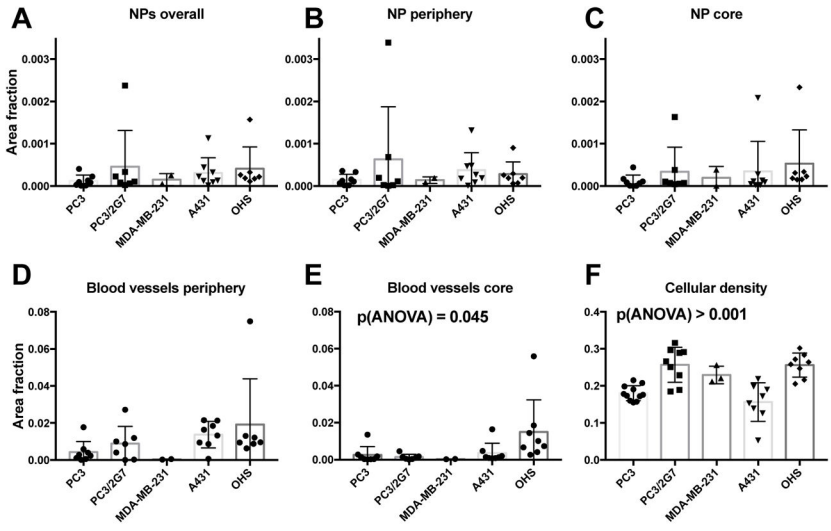

Fig. 7.

Fluorescence image analysis of the 5 tumor models determining: A–C: amount of nanoparticle in the whole tumor, tumor periphery (outer 1mm) and tumor core. D: Area fraction of nuclei, E and F; blood vessel area fraction in the tumor periphery and core. Each datapoint represent one tumor and mean and standard deviation is shown.

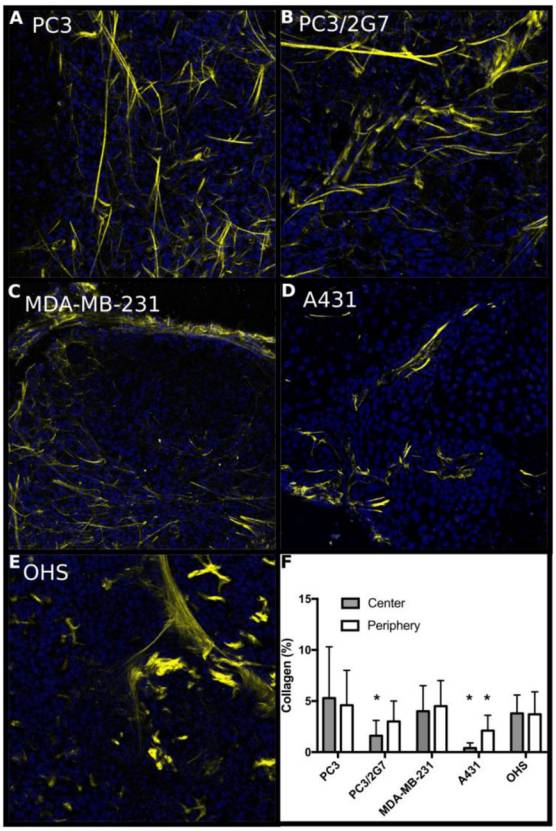

Fig. 8.

Collagen content in the 5 tumor models imaged with SHG. A–E; representative images from the periphery of the tumors. F; area fraction (%) of collagen in the center and periphery of the various tumors. Error bars show standard deviation from 36 images/tumor type (periphery) and 12 images per tumor type (central part), * indicates values significantly different ($p<0.05$, one-way ANOVA) from the other models.

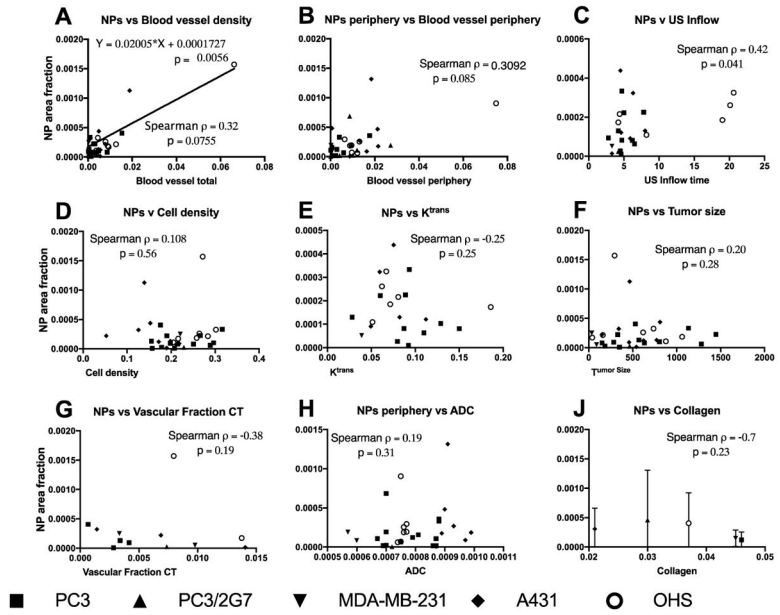

Fig. 9.

Plots of NP accumulation vs different parameters. Each datapoint represent one tumor except for J which shows mean and standard deviation from 6 sections in 2 tumors from each type. Spearman rank correlations are shown and was significant for NP vs Inflow time. A linear relation was found between NPs and blood vessel density.

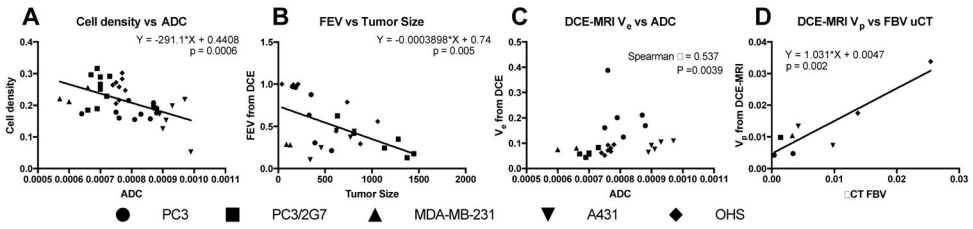

Fig. 10.

Plots of A; Cell density vs ADC, B; FEV from DCE-MRI vs Tumor size, C; Extravascular and extracellular compartment from DCE-MRI vs ADC, D; Perfusion fraction from DCE-MRI vs FBV from μCT.

Table 1

Number of animals included in the analysis of different parts of the study.

Tumor	DCE- MRI	DW- MRI	US	CT	Microscopy
PC3	7	11	7	5	8
PC3/2G7	6	9	6	4	7
MDA-MB-231	2	3	2	3	2
A431	5	8	6	2	8
OHS	8	9	7	3	7

Table 2

Summary of characteristics of the tumor models.

Measured parameter	PC3	PC3/2G7	MDA-MB- 231	A431	OHS
NP accumulation	**Low**	**Low-high**	**Low**	**Medium**	**Medium**
Microbubble inflow time	**Short**	**Medium**	**Short**	**Medium**	**Long**
Collagen density	**High**	**Low**	**Medium**	**Low**	**Medium**
Blood vessel density (microscopy)	**Medium**	**Medium- high**	**Low**	**Medium- high**	**High**
Blood vessel density total (μ-CT)	**Low**	**Medium**	**Medium**	**Medium**	**High**
Blood vessel density in periphery (μ-CT)	**Low**	**High**	**Low**	**Medium**	**High**
Diffusivity (ADC)	**High**	**Medium**	**Low**	**High**	**Medium**
Distribution of MRI contrast agent (FEV)	**High**	**Medium**	**Low**	**Low**	**High**
K^{trans}	**Medium**	**High**	**Low**	**Medium**	**Medium**
Cell density	**Low**	**High**	**High**	**Low**	**High**